Research Square

Preprints are preliminary reports that have not undergone peer review.
They should not be considered conclusive, used to inform clinical practice,
or referenced by the media as validated information.

Heat transfer patterns of marine heatwaves with distinct vertical structures in the southwestern East Sea (Japan Sea)

Jae-Heon Lee
ARA Consulting & Technology
Cheol-Ho Kim
ARA Consulting & Technology
Do-Youn Kim
ARA Consulting & Technology
You-Soon Chang
yschang@kongju.ac.kr

Kongju National University

Article

Keywords: Decomposition, Lateral boundary forcing, Marine heatwaves, Vertical structure

Posted Date: November 12th, 2026

DOI: https://doi.org/10.21203/rs.3.rs-11285976/v1

License: This work is licensed under a Creative Commons Attribution 4.0 International License.
Read Full License

Additional Declarations: No competing interests reported.

Heat transfer patterns of marine heatwaves with distinct vertical structures in the southwestern East Sea (Japan Sea)

Jae-Heon Lee[1], Cheol-Ho Kim[1], Do-Youn Kim[1,2], You-Soon Chang[2*]

[1]ARA Consulting & Technology, Incheon, South Korea
[2]Department of Earth Science Education, Kongju National University, Gongju, South Korea

*** Corresponding author:** You-Soon Chang (yschang@kongju.ac.kr)

Abstract

Recent studies have shown that marine heatwaves (MHWs) with similar surface signals can have distinct subsurface vertical structures; however, the processes associated with these differences remain an open question. MHW heat budgets have predominantly been examined at the mixed-layer scale, and the components of oceanic forcing in the subsurface have received less attention. We classified MHWs in the southwestern East Sea by their vertical structures and analyzed the associated heat transfer patterns. By applying K-means clustering to MHW events identified from detrended sea surface temperatures, we categorized the vertical structures into four types: subsurface-intensified, deep, shallow, and subsurface-reversed. We then analyzed the heat budget of each type by decomposing the lateral heat flux into dynamical (associated with velocity anomaly) and thermodynamical (associated with temperature anomaly) components. In the shallow type, the net surface heat flux term contributed most to the warming. In the subsurface-intensified and deep types, the dynamical component contributed more to the warming than the thermodynamical component, particularly in the subsurface-intensified type. In the subsurface layer, however, the thermodynamical component exerted a cooling effect, partially offsetting the dynamical warming. This study demonstrates that the dynamical and thermodynamical contributions to the lateral heat flux vary substantially among MHW types.

Keywords: Decomposition, Lateral boundary forcing, Marine heatwaves, Vertical structure

Introduction

Marine heatwaves (MHWs) are extreme oceanic events characterized by anomalously high water temperatures persisting for several days or longer in a specific region. They cause severe damage across marine ecosystems, including coral bleaching, loss of kelp forests, and the collapse of fishery resources[1–3]. Under global warming, the frequency and intensity of MHWs have substantially increased[1,4]. However, because the manifestation of MHWs varies by region, predicting their impacts requires an understanding of the conditions and processes under which MHWs occur in a given region.

The East Sea (Japan Sea) (hereafter East Sea), a semi-enclosed marginal sea in East Asia, is characterized by the complex interactions of the Tsushima Warm Current carrying high-temperature and high-salinity water, its branch the East Korea Warm Current, the North Korea Cold Current transporting cold water from the north, mesoscale eddies, and seasonal stratification. In addition, the East Sea is often regarded as a miniature ocean because it exhibits subtropical and subpolar circulations as well as a thermohaline circulation similar to those in the open ocean, but on a smaller scale. Its relatively short response timescale allows signals of global warming to emerge more rapidly, making

the East Sea a valuable natural laboratory for investigating oceanic responses to climate change. In this region, surface warming exceeding the global average has been reported[5,6], and recent studies have also consistently shown a rapid increase in the frequency and intensity of MHWs[6–9].

Traditionally, MHWs have been defined as periods when the daily sea surface temperature (SST) exceeds the 90th percentile of a fixed climatological baseline (typically over a past 30-year period) for at least five consecutive days[10]. Maintaining this fixed baseline under continuous global warming, however, leads to a quasi-permanent MHW state where temperatures persistently exceed the threshold[11–13]. Thus, a substantial portion of the observed MHW increase against a fixed baseline is attributable to background warming[14,15]. Because the baseline elevation is more pronounced in regions with faster warming rates, this issue can be more severe in the East Sea. Accordingly, recent studies have defined MHWs after removing the long-term trend from the SST time series, thereby isolating variations distinct from background warming[11,13,14,16,17]. In the East Sea, however, few MHW studies have separated background warming to examine the contribution of internal variability.

MHWs are generally detected using satellite-based SST observations, but surface signals alone are insufficient to capture the internal thermal structure of the ocean[16]. Recent studies analyzing subsurface vertical profiles have reported that the vertical structures during MHWs can be classified into several types, with each type showing a different pattern of evolution[18,19]. Subsurface intensification, where the intensity of summer MHWs is greater below the sea surface than at the surface, has also been identified in the East Sea[20]. The involvement of oceanic advection in extreme subsurface temperatures has been reported across various regions[8,16,21], and a global Earth system model study has suggested that advection drives subsurface MHWs[22]. If the processes acting at the surface and subsurface differ, the subsequent question is how the contributions of heat transfer factors vary among MHWs with different vertical structures.

The heat transfer factors of temperature change during MHWs are atmospheric forcing (surface heat flux) and oceanic forcing (lateral heat flux). Both global diagnostic studies and regional case studies have evaluated the relative contributions of these two factors[9,15,16,19,22–26]. In these studies, oceanic forcing has conventionally been treated as a single term. However, this term consists of three components: the dynamical component associated with velocity anomalies, the thermodynamical component associated with temperature anomalies, and the nonlinear component that reflects their simultaneous changes. Although all three components alter water temperature, they reflect different oceanic states; thus, a single term cannot identify which component contributed. This decomposition is based on Reynolds decomposition, which separates each variable into mean and anomalous components, and has long been used in studies of ocean heat transport and heat content variability[27–31]. However, such decompositions have typically been conducted at the mixed-layer scale, and the classification of MHWs has relied primarily on surface temperature change patterns or dominant driving factors. In a vertically resolved heat budget, how each component contributes to MHWs with different subsurface vertical structures has not yet been thoroughly examined.

Therefore, we classified MHWs occurring in the southwestern East Sea according to their subsurface vertical structures and compared the magnitude and sign of each heat transfer factor among types. Specifically, we (1) identified MHW events from detrended SSTs to exclude background warming, (2) classified MHW types based on subsurface vertical temperature anomaly profiles, and (3) examined vertical and horizontal distribution characteristics for each type. We then (4) compared the contributions of surface heat flux and lateral heat flux across depth layers and (5) examined differences among types by decomposing the lateral heat flux into dynamical, thermodynamical, and nonlinear

components. This approach classifies MHWs, which cannot be distinguished by surface temperature alone, by their vertical structures and identifies the combination of heat transfer factors corresponding to each structure. Through this, the present study aims to treat MHWs not merely as surface events, but as events with inherent vertical structures.

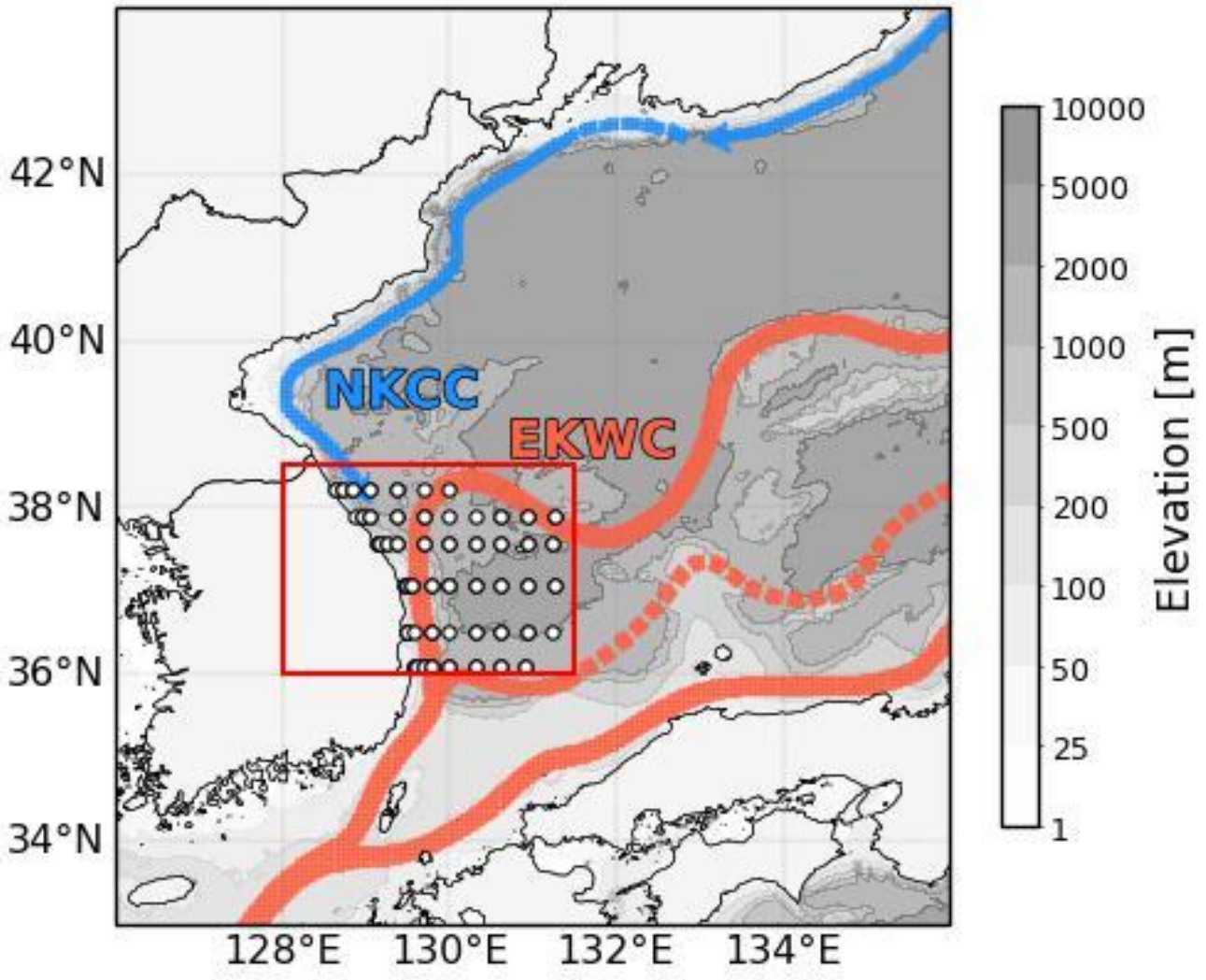


Fig. 1. Study area and major currents in the East Sea. The red box indicates the analysis domain (128°–131.5°E, 36°–38.5°N). Red and blue lines indicate the paths of the East Korea Warm Current (EKWC) and the North Korea Cold Current (NKCC), respectively. Gray shading represents bathymetry from the GEBCO gridded dataset, and white dots mark the NIFS serial oceanographic observation stations along lines 102–107. Current paths are available at https://www.khoa.go.kr/oceandata/oceaninfo/map.do.

Results

Detection of surface MHWs

A total of 35 MHW events were identified in the southwestern East Sea (128°–131.5°E, 36°–38.5°N; Fig. 1; see Methods). These events occurred in 19 of the 33 years analyzed. The annual frequency

averaged 1.1 events year^{-1} (range: 0–4 events year^{-1}), with a maximum of four events in both 2001 and 2012. The mean duration was 12.7 days (annual mean range: 5–28.5 days), with the longest duration observed in 1994. The mean maximum intensity was 2.5 °C (annual mean range: 1.7–3.9 °C), and the mean cumulative intensity was 28.4 °C·day (annual mean range: 7.8–85.6 °C·day) (Fig. 2a–d).

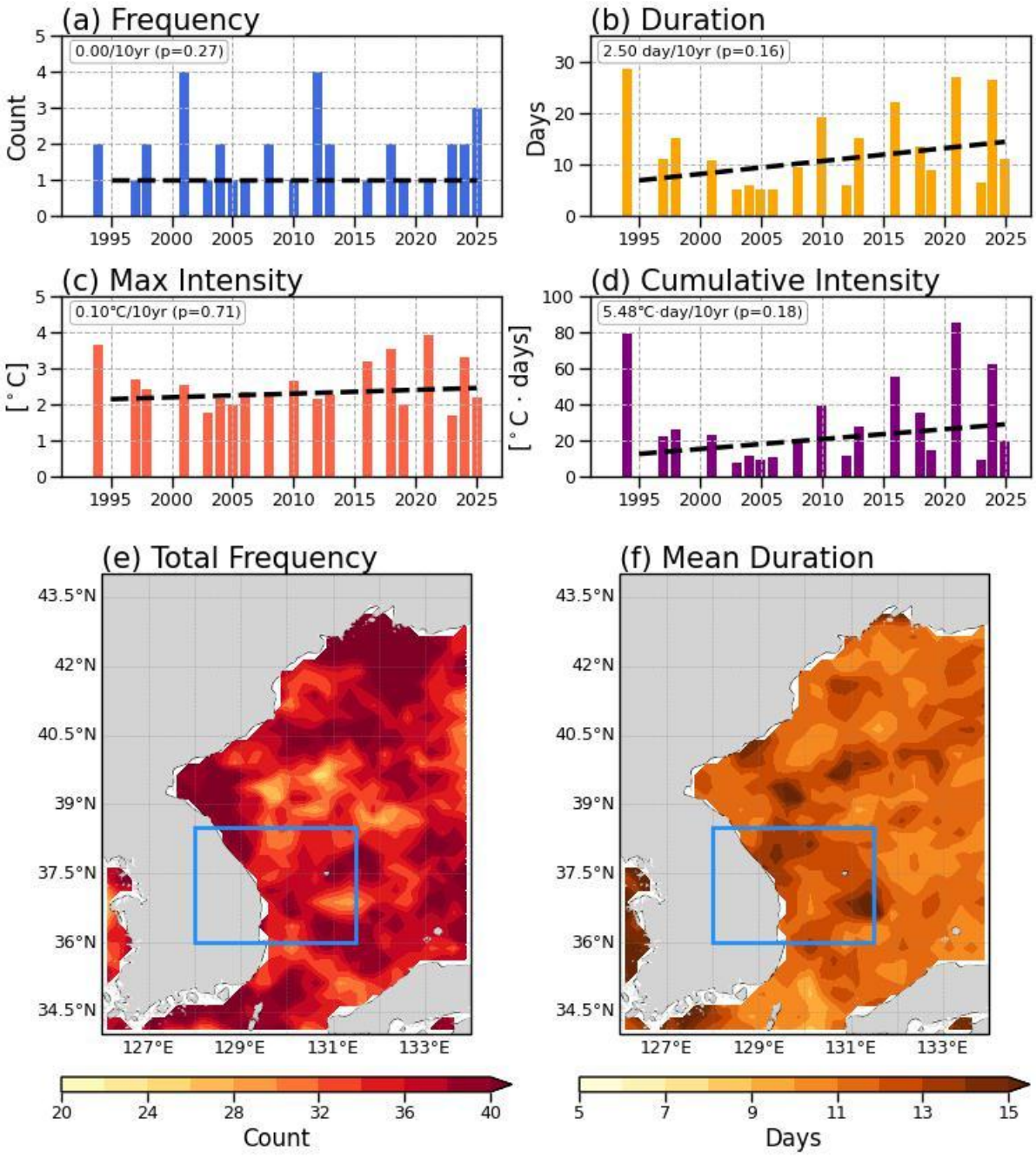


Fig. 2. Characteristics of MHW events extracted using detrended SST: (a) total frequency, (b) mean duration, (c) mean maximum intensity, (d) mean cumulative intensity. Dashed lines indicate the Theil–Sen slope estimated without 1994; the trends are not statistically significant (Mann–Kendall, $p > 0.15$). The corresponding slopes and p-values are provided in the legend. (e) and (f) show the total frequency and mean duration at each grid cell, respectively. The blue box indicates the analysis domain. Here, "mean" refers to the average over MHW events.

To assess the long-term changes, we performed an outlier-robust Theil–Sen trend analysis and a Mann–Kendall test on the annual mean values of the four metrics derived from the detrended SST. The trend analysis for frequency included all 33 years (including zero-event years), whereas the analysis for the other three metrics was restricted to the 19 years with MHWs. Over the entire study period, the Theil–Sen slopes were 0 events decade^{-1} (p = 0.89) for frequency, 0.88 days decade^{-1} (p = 0.50) for duration, −0.03 °C decade^{-1} (p = 0.89) for maximum intensity, and 3.37 °C·day decade^{-1} (p = 0.49) for cumulative intensity; none were statistically significant (Fig. 2a–d). Annual mean durations exceeding 20 days were recorded in four years (1994, 2016, 2021, and 2024), three of which occurred after 2010. With 1994 excluded (the only early year with such a long duration), the slopes increased to 2.50 days decade^{-1} (p = 0.16) for duration and 5.48 °C·day decade^{-1} (p = 0.18) for cumulative intensity, but neither was statistically significant.

Fig. 2e and 2f show the spatial distributions of the total frequency and mean duration for all events, respectively. The spatial variability of the total frequency and mean duration within the analysis domain (blue box) was small, with a coefficient of variation of 0.09 for each. The mean number of events detected at individual grid cells (35.8 events) was consistent with the number identified from the domain-averaged SST (35 events). In addition, on the peak day of each event, an average of 71% of the grid cells within the analysis domain were in an MHW state (range: 23–100%). These results indicate that most of the detected MHWs occurred coherently across the analysis domain. However, a few events showed lower spatial coherence.

Vertical and horizontal distribution characteristics by type

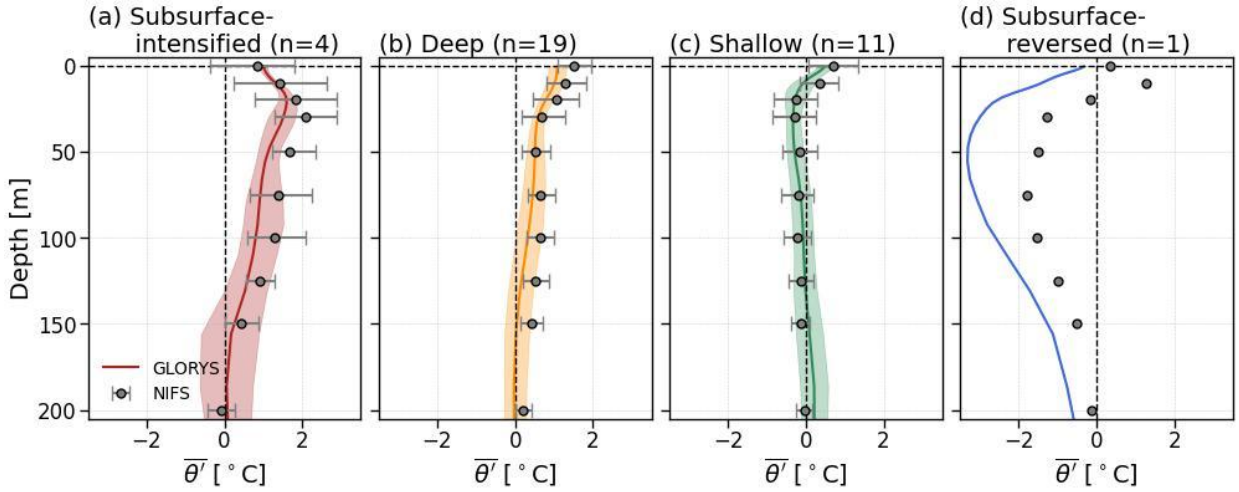


Fig. 3. Composite vertical profiles of temperature anomalies for each MHW type. (a) Subsurface-intensified (n = 4), (b) deep (n = 19), (c) shallow (n = 11), and (d) subsurface-reversed (n = 1) types. Solid lines and shading indicate the GLORYS composite mean and its bootstrap 95% confidence interval, respectively, averaged over ±30 days around the MHW peak day. Gray dots and error bars represent the mean and 95% confidence interval of NIFS observations at each standard depth within the same window. No confidence interval is shown for the subsurface-reversed type, which consists of a single event.

The subsurface thermal structures during MHWs were classified into four types: subsurface-intensified, deep, shallow, and subsurface-reversed. The type names follow the naming convention of Zhang et al.[18]. Fig. 3 shows the composite vertical profiles of the GLORYS and NIFS temperature anomalies for each type. The profiles were temporally averaged over a ±30-day window centered on the MHW peak day. The subsurface-intensified type, which exhibits a maximum warming anomaly in the subsurface layer, accounted for 4 of the 35 events. The deep type is characterized by a surface warming anomaly that monotonically decreases with depth and was identified in 19 events. The shallow type, in which warming is confined to the surface and decreases rapidly with depth, appeared in 11 events. The single subsurface-reversed event, which occurred in August 2006, was detected as a short-lived surface MHW but exhibited a cold anomaly in the subsurface (Supplementary Fig. S1).

For the subsurface-reversed type (n = 1), the ±30-day mean surface temperature anomaly is negative (Fig. 3d). This event lasted 5 days, shorter than the mean of all events (12.7 days). Because of this short duration, cooler conditions outside the event outweigh its warm peak signal in the ±30-day average. A previous study noted that this type tends to be shorter than even the shallow type[19].

We tested the sensitivity of the composite profiles to the averaging window (±10, ±20, and ±30 days). The vertical structure of each type is consistent across window sizes (Supplementary Fig. S2), indicating that the composite vertical structures are robust to the choice of averaging window. Window size affects only the magnitude of the maximum anomaly, which is larger for shorter windows (at 20–30 m for the subsurface-intensified type and at the surface for the other types).

We compared the GLORYS composite profiles with independent in situ profiles from NIFS (Fig. 3). For the subsurface-intensified, deep, and shallow types, the GLORYS mean falls within the 95% confidence intervals of the NIFS profiles at 90% of the standard depths. In all three types, the signs of the anomalies and their vertical gradients are consistent between the two datasets. In the subsurface-reversed type, the GLORYS profile is on average 1.38 °C colder than the NIFS profile. Because this type comprises a single event, confidence intervals could not be calculated. Therefore, this type is presented for reference only and is excluded from cross-type comparisons and overall syntheses.

Fig. 4 illustrates the GLORYS temperature anomaly fields at depths of 0, 50, 100, and 150 m, averaged over the same ±30-day window. At the surface (0 m), the SST anomalies from OI SST, averaged in the same manner, are superimposed as contours. The domain-averaged surface anomalies of GLORYS are lower than or similar to those of OI SST in all three types, with differences (GLORYS – OI SST) ranging from −0.25 to 0.03 °C; the difference is largest for the shallow type.

At the surface, the subsurface-intensified and deep types show positive anomalies exceeding 1 °C across the entire analysis domain, with larger anomalies in the northwestern part. The shallow type exhibits smaller anomalies without a clear spatial pattern (Fig. 4a–c). The differences among the types increase with depth. At 50 and 100 m, local anomalies in the subsurface-intensified and deep types exceed 2 °C, larger than the maximum surface anomalies. For the shallow type, positive anomalies mostly disappear at 50 m, and weak negative anomalies appear below this depth. Thus, unlike the shallow type, the subsurface-intensified and deep types exhibit a spatial contrast between the surface and the subsurface. Their surface anomalies are broadly distributed, whereas their subsurface positive anomalies are confined to the northwestern and southeastern parts of the domain, each approximately 100 km wide.

The subsurface-reversed type (n = 1) shows negative anomalies (Fig. 4d). Strong negative anomalies exceeding 2 °C dominate below 50 m, but positive anomalies reappear locally at 100–150 m, for

example in the northwestern part.

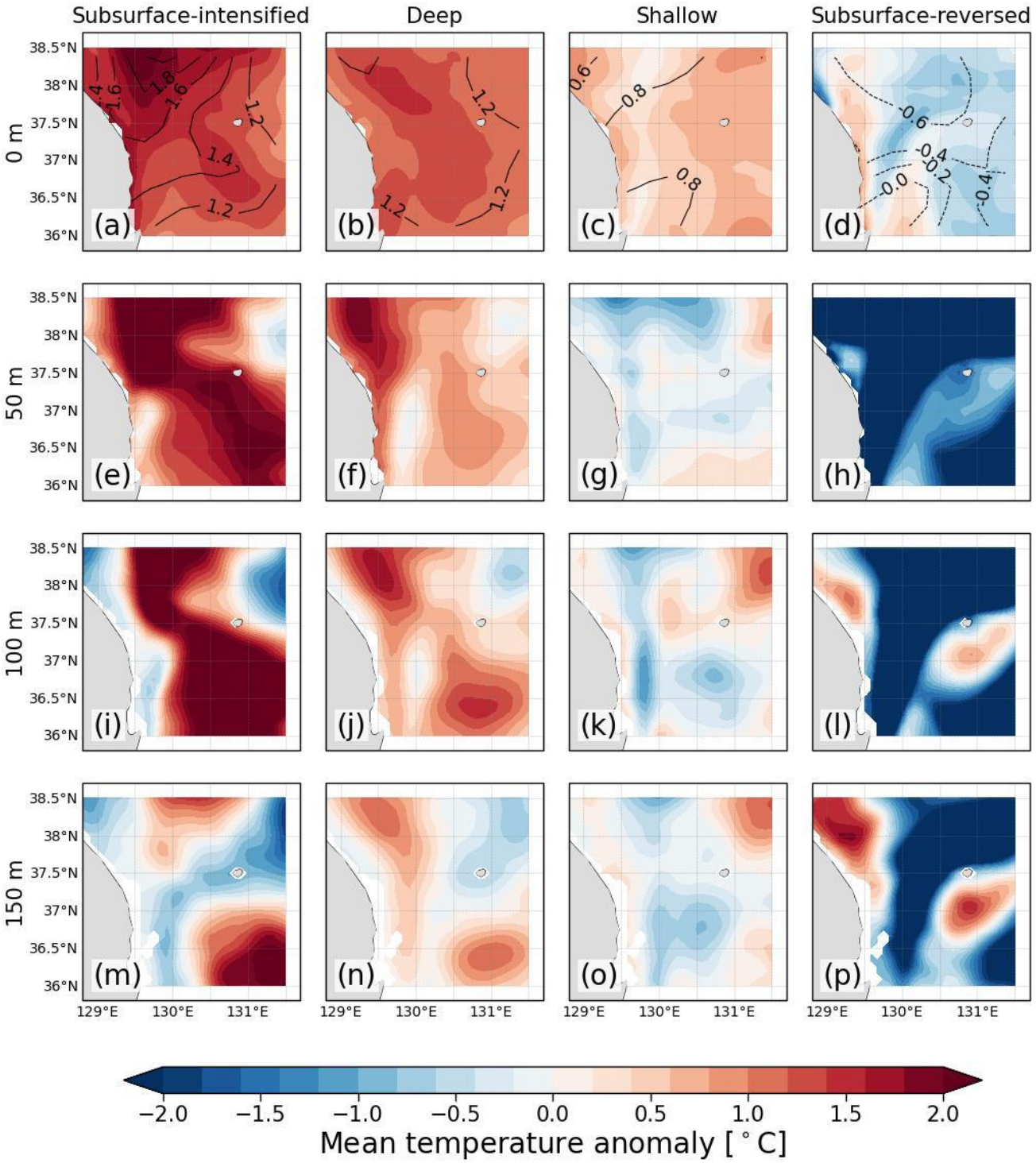


Fig. 4. Composite temperature anomaly fields for each MHW type at different depths. (a–d) GLORYS temperature anomalies (shading) at the surface for the subsurface-intensified, deep, shallow, and subsurface-reversed types, with OI SST anomalies (contours) superimposed. (e–h), (i–l), and (m–p) Same as (a–d) but at 50, 100, and 150 m, respectively. All fields are averaged over ±30 days around the MHW peak day.

Heat transfer patterns by type

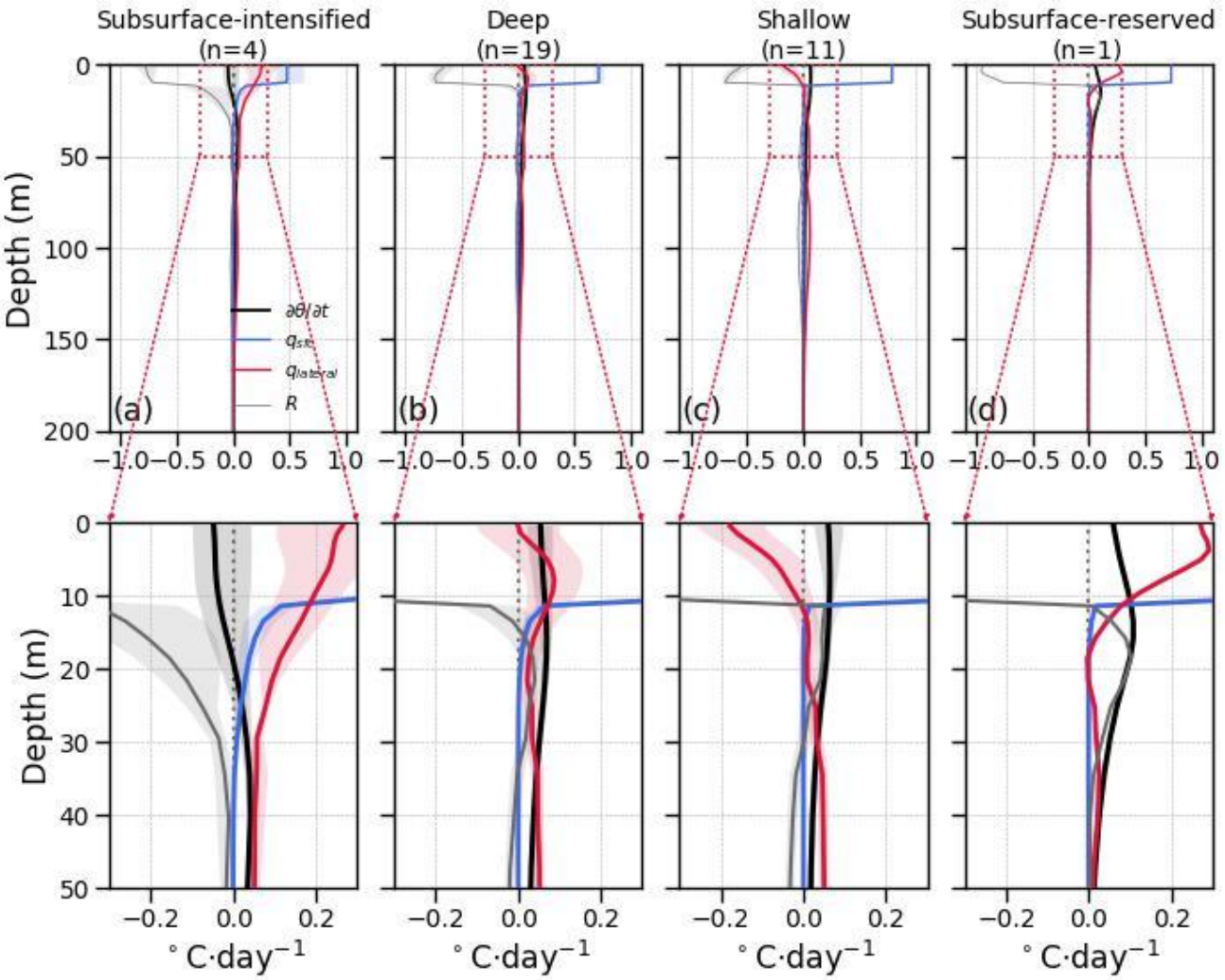


Fig. 5. Composite vertical profiles of the full heat budget terms for each MHW type. (a) Subsurface-intensified, (b) deep, (c) shallow, and (d) subsurface-reversed types. Black, blue, red, and gray lines indicate the temperature tendency ($\partial\theta/\partial t$), surface heat flux term (q_{sfc}), lateral heat flux term ($q_{lateral}$), and residual (R), respectively. Shading indicates bootstrap 95% confidence intervals. All terms are averaged over ±30 days around the MHW peak day.

Fig. 5 shows the vertically resolved full heat budget averaged over the ±30-day window centered on the peak day for each MHW type. Because this window includes both pre-peak and post-peak periods, the total temperature tendency is small. However, it exhibits distinctly different patterns across the types. Its maximum occurs at 40, 16, and 8 m for the subsurface-intensified, deep, and shallow types, respectively. This sequence is consistent with the vertical structure classification presented in Fig. 3. The subsurface-reversed type (n = 1) appears to have a maximum at about 15 m within the mixed layer.

In the mixed layer, q_{sfc} and R retain their signs across all types but differ in magnitude: q_{sfc}

makes a positive contribution (0.48–0.79 °C day^{-1}), whereas R makes a negative contribution of equal or greater magnitude. Because q_{sfc} is constrained within the mixed layer of each event, the composite q_{sfc} reaches zero exactly at the maximum mixed-layer depth of each type. This depth is greatest in the subsurface-intensified type (34 m), followed by the deep (22 m) and shallow (16 m) types. The primary factor distinguishing the types is $q_{lateral}$, whose sign within the mixed layer varies across the types. In the subsurface-intensified type, $q_{lateral}$ represents a positive contribution (0.23 °C day^{-1}), nearly half of q_{sfc}. In the deep type, it accounts for only one-fourth of q_{sfc}, whereas in the shallow type it makes a negative contribution, which partially offsets q_{sfc}. For the subsurface-reversed type (n = 1), q_{sfc} and R within the mixed layer resemble those of the other three types, whereas $q_{lateral}$ shows different behavior.

During the boreal summer, the ocean almost always warms due to strong shortwave radiation. Against this seasonal background, the lateral heat flux exhibits vertical structures that differ clearly among the types, indicating that it aggregates thermodynamical processes and dynamical processes. In contrast, the surface heat flux, which arises solely from atmospheric forcing, differs among types only in magnitude. The lateral heat flux must therefore be decomposed to identify which physical component contributes most in each type.

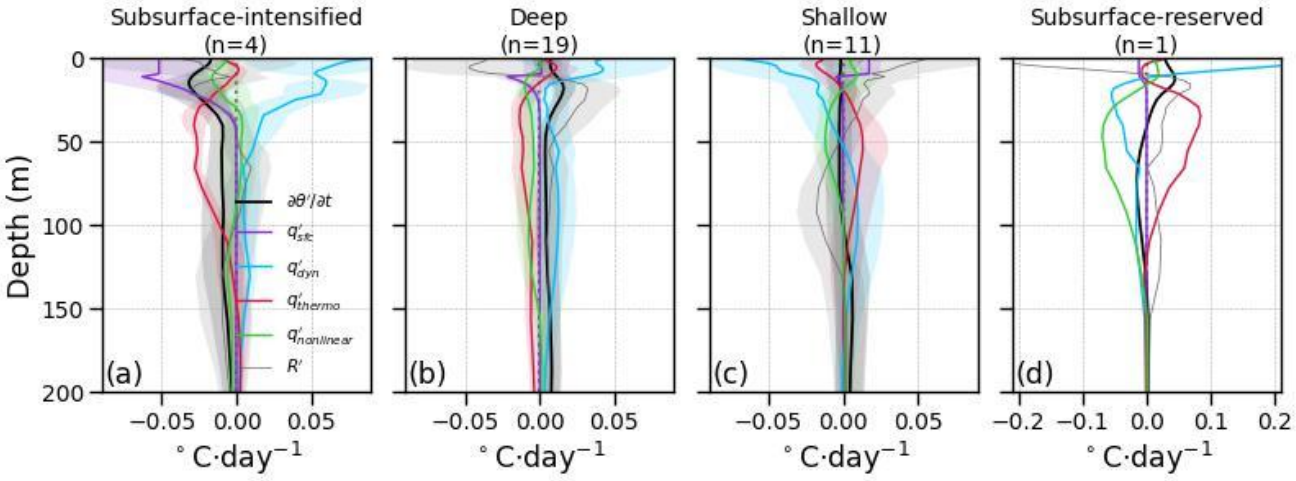


Fig. 6. Composite vertical profiles of the anomalous heat budget terms for each MHW type. (a) Subsurface-intensified, (b) deep, (c) shallow, and (d) subsurface-reversed types. Lines indicate the temperature anomaly tendency ($\partial\theta'/\partial t$, black solid), anomalous surface heat flux term (q'_{sfc}, purple solid), anomalous residual (R', gray dotted), and the dynamical (q'_{dyn}, blue solid), thermodynamical (q'_{thermo}, red solid), and nonlinear ($q'_{nonlinear}$, green solid) components of the anomalous lateral heat flux. All terms are averaged over ±30 days around the MHW peak day. Shading indicates bootstrap 95% confidence intervals.

Fig. 6 presents the vertically resolved anomalous heat budget averaged over the same window for each type. The sum of q'_{dyn}, q'_{thermo}, and $q'_{nonlinear}$ is equivalent to $q_{lateral}$ minus its climatological mean component. Each term indicates whether the respective forcing was stronger or weaker than the climatology. For example, a positive q'_{sfc} implies that the combined effect of its components heated the ocean more intensely than usual.

In the mixed layer, q'_{dyn} is the dominant component among the lateral terms across all four types.

Specifically, its positive contribution is most pronounced in the subsurface-intensified type, followed by the deep type, whereas it contributes to cooling in the shallow type. Depending on the type, other terms either offset or reinforce this contribution. For the subsurface-intensified type, q'_{sfc} offsets most of q'_{dyn}. For the shallow type, the cooling effect of q'_{dyn} is counteracted by positive contributions from q'_{sfc} and R'. In contrast, for the deep type, q'_{sfc} is near zero, and the q'_{dyn} contribution is mostly offset by R'.

In the subsurface layer, the composition of the anomalous heat budget changes notably; the influence of q'_{sfc} and q'_{dyn} diminishes or disappears, and q'_{thermo} becomes the dominant contributor. In the subsurface-intensified type, q'_{thermo} reaches nearly three times the magnitude of q'_{dyn}. The sign of q'_{thermo} also varies by type, appearing negative in the subsurface-intensified and deep types but positive in the shallow type. In the deep and shallow types, $q'_{nonlinear}$ provides a negative contribution that compensates for the positive tendencies of q'_{dyn} and q'_{thermo}, respectively. However, it remains small across all depths in the subsurface-intensified type. For the subsurface-reversed type (n = 1), q'_{dyn} and R' offset each other with nearly identical magnitudes in the mixed layer, whereas q'_{thermo} and $q'_{nonlinear}$ exhibit opposite signs in the subsurface.

Although the mixed-layer q_{sfc} is positive for all three primary types in the full heat budget (Fig. 5), q'_{sfc} is −0.05 °C day^{-1} for the subsurface-intensified type and near zero for the deep type. Thus, in these two types, the surface heat flux is not stronger than its climatological mean. Only the shallow type exhibits positive values in both budget forms. Below a depth of 100 m, the contributions of all terms decrease to less than half of those in the upper layers. However, in the deep type, q'_{dyn} remains the largest among the three lateral components and is distinguishable from zero below 92 m.

Evolution in heat transfer patterns

Although Fig. 6 illustrates the representative vertical structure for each type, the ±30-day average centered on the peak day masks temporal differences in the contributions of each term before and after the peak. Fig. 7 shows the anomalous heat budget for each type across the pre-peak (15 to 6 days prior to the peak), peak (±5 days), and post-peak (6 to 15 days after the peak) periods. These periods were defined relative to the peak day, rather than to the start and end dates of individual events, to compare the heat budget at the same lags across events of different durations (see Methods). In the subsurface-intensified and deep types, warm anomalies in the upper 100 m tend to persist after the peak (Supplementary Fig. S1).

In the subsurface-intensified type, q'_{dyn} maintains a positive contribution within the mixed layer throughout the entire three periods, exhibiting the largest absolute magnitude among the three lateral components. During the pre-peak period, it reaches a maximum of 0.19 °C day^{-1} but decreases sharply to less than half its magnitude below 10 m. In the peak period, the positive tendency of q'_{dyn} attenuates, yet it provides a relatively uniform positive contribution down to 30 m and extends below 50 m. During the post-peak period, it intensifies again near the surface, and its positive contribution persists down to the depths reached during the peak period. This positive contribution from q'_{dyn} is largely offset by q'_{sfc} and R'. Interestingly, while q'_{thermo} reinforces q'_{dyn} with a positive contribution in the mixed layer during the pre-peak period, it transitions to a negative contribution during the peak and post-peak periods, thereby counteracting q'_{dyn}.

In the deep type, the directions of change in the mixed layer and the subsurface layer are opposite. Within the mixed layer, q'_{sfc} makes a positive contribution during the pre-peak and peak periods but transitions to a negative contribution during the post-peak period, and the temperature anomaly tendency evolves similarly. In contrast, in the subsurface layer, q'_{dyn} increases continuously throughout the three periods, and the temperature anomaly tendency remains positive through the post-peak period. q'_{thermo} provides a negative contribution in the subsurface layer across the entire three periods, reaching its maximum magnitude during the post-peak period.

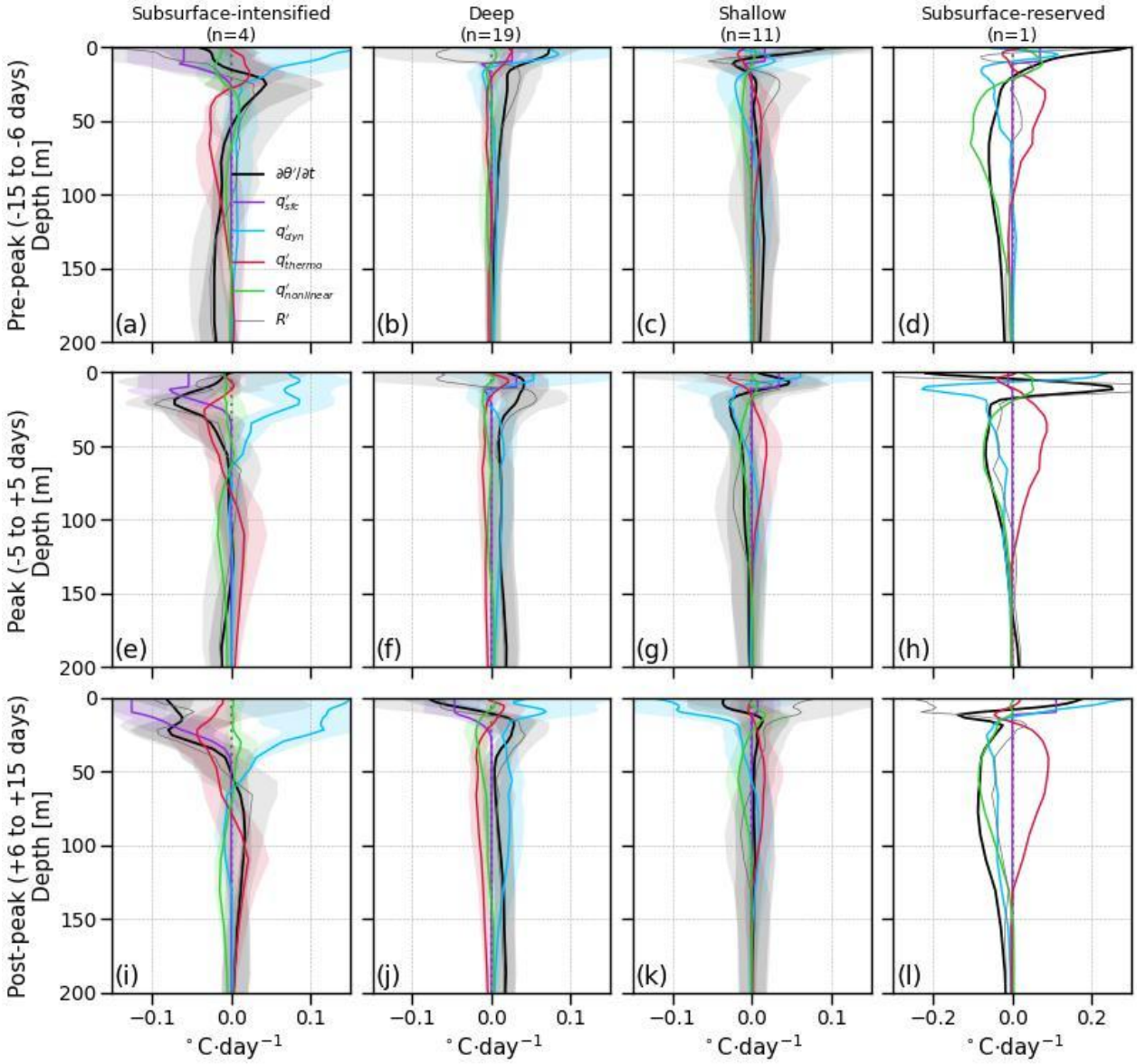


Fig. 7. Anomalous heat budget terms for each MHW type during the pre-peak (15–6 days before the peak), peak (±5 days), and post-peak (6–15 days after the peak) periods. Same as Fig. 6 but averaged over the periods.

In the shallow type, the behavior of each term throughout the three periods differs distinctly from that in the other types. q'_{sfc} provides a positive contribution during the pre-peak and peak periods, and the temperature anomaly tendency is also positive. During these periods, q'_{dyn} also yields a

positive contribution, reinforcing the effect of q'_{sfc}. In the post-peak period, q'_{dyn} corresponds to the cooling of the mixed layer, which had warmed during the peak period. In contrast, in the subsurface layer, q'_{thermo} consistently provides a positive contribution, while q'_{dyn} and $q'_{nonlinear}$ make negative contributions, partially offsetting the influence of q'_{thermo}. For the subsurface-reversed type (n = 1), q'_{thermo} and $q'_{nonlinear}$ in the subsurface layer consistently counteract each other across the three periods. Notably, during the post-peak period of the subsurface-intensified and deep types, q'_{dyn} continues to provide a positive contribution even as the overall temperature tendency becomes negative. This indicates that the decay of these types is not attributable to a weakening of the anomalous lateral flow.

Discussion

We classified surface MHWs in the southwestern East Sea into four types according to their vertical structures (subsurface-intensified, deep, shallow, and subsurface-reversed) and examined the associated heat budgets. In the subsurface-intensified and deep types, the anomalous lateral heat flux contributed more to warming than the anomalous surface heat flux. Decomposition of this term showed that the warming in these two types was associated mainly with the velocity anomaly (the dynamical component) rather than with the temperature anomaly (the thermodynamical component). In the subsurface-intensified type, the dynamical component contributed to warming throughout the pre-peak, peak, and post-peak periods, whereas the thermodynamical component contributed to cooling in the subsurface layer, partially offsetting the dynamical warming.

The classification procedure follows the framework of a previous study in the East Sea[19], in which domain-averaged temperature anomaly profiles for ±30 days around the peak day were configured into a time–depth array for clustering. However, our analysis differs in that events were identified from detrended SSTs and in the reanalysis product, target region, and analysis period. The inertia curve for K-means clustering does not exhibit a distinct elbow, and silhouette scores remain below 0.2 across the analyzed k range (Supplementary Fig. S3). This implies that the vertical structures of MHWs exist on a spatiotemporally continuous distribution. Given this continuity, we selected $k = 4$ on the basis of the physical validity of the classified structures. At $k = 4$, the subsurface-intensified type separates as an independent cluster, and its structure is supported by both the reanalysis and the NIFS in situ observations. At $k = 3$, this subsurface maximum merges into the deep type, and its distinct characteristics are obscured (Supplementary Fig. S4). Specifically, the 17 events in the deep-warming cluster at $k = 3$ split into the deep (13 events) and subsurface-intensified (4 events) types at $k = 4$, and the remaining 6 deep-type events are reassigned from the shallow type. The deep, shallow, and subsurface-reversed structures do not change markedly with k.

These four structures correspond to the classification framework established in a previous global-scale MHW study[18]. Because $k = 4$ necessarily yields four clusters, this correspondence rests not on the number of clusters but on the profile shape of each cluster. According to the previous study[18], the deep type dominates in subtropical and subpolar regions, the shallow type is concentrated in mid-to-high latitudes, and the two subsurface types primarily occur in the tropics (including the Kuroshio and its extension for the subsurface-intensified type). Our study area is located around 37°N, and our finding—where the deep type accounts for more than half of the total events, followed by the shallow type, with the subsurface-intensified and subsurface-reversed types remaining a minority—aligns well with their report. Moreover, all four types occurred within a single coastal region, which allows the

heat transfer patterns inherent in each event to be compared without the confounding effects of disparate geographic baseline conditions.

The surface heat flux contributed positively in all types, but its anomaly contributed negatively in the subsurface-intensified type. Once the seasonal background of continuous summer atmospheric heating is removed, the atmospheric warming during these events is revealed to be weaker than its climatology. This may reflect enhanced oceanic latent heat loss (a negative feedback) in response to elevated surface temperature[24,32,33], and indicates that atmospheric forcing is not the primary contributor to warming in the subsurface-intensified type. However, this negative contribution does not span the entire three periods in all types; in the deep type, it is positive during the pre-peak and peak periods and becomes negative during the post-peak period.

This type-dependent partitioning of atmospheric and oceanic roles is consistent with previous findings in the East Sea. Surface-confined MHWs are generated by heat trapping at the surface due to weakened winds and increased shortwave radiation, whereas MHWs with warming in the upper 200 m are dominated by horizontal advection, with a small net surface heat flux contribution[19]. At the global scale, the shallow type is associated with surface heat flux and the deep type with advection, whereas the two subsurface types are linked to other oceanic processes such as thermocline variations, mesoscale eddies, and strong current systems[18]. In addition, several studies reported the critical role of ocean dynamics in current-dominated regions[22,25].

Unlike the conventional practice of treating the lateral heat flux as a single term, this study decomposed it into dynamical and thermodynamical components and compared them among MHW types. Even when the lateral term has the same magnitude, velocity anomaly and temperature anomaly represent entirely different oceanic states. The dominance of the dynamical component in the subsurface-intensified and deep types is consistent with reports that velocity variations in the currents through the Korea–Tsushima Strait have a far greater influence on the East Sea heat content variations than temperature variations do[30]. Meanwhile, the cooling by the thermodynamical component in the subsurface layer indicates that the inflow of warm currents does not act solely as a warming factor, even during extreme MHWs, which demands a more multidimensional perspective on MHW processes. Extending previous studies that focused on mixed-layer analyses or on identifying the dominant heat budget terms[21,24,34], this study shows how the composition of the lateral boundary forcing components varies with the vertical structure of MHWs.

Several limitations should be noted. Because extreme events are rare (four subsurface-intensified events and one subsurface-reversed event), the composites for these types may reflect the characteristics of individual events. The uncertainty of GLORYS in reproducing cold structures, reported in previous studies, also constrains the interpretation of the subsurface-reversed type[19,35]. In addition, because the lateral heat flux was formulated as fluxes across horizontal boundaries, vertical exchanges are incorporated into the residual. This residual provides a strong negative contribution comparable in magnitude to the surface heat flux within the mixed layer, but it was not decomposed further because this study was designed to analyze the composition of the lateral heat flux. Quantifying its individual processes, such as vertical mixing and entrainment, remains a task for future research. Despite these limitations, our results show that MHWs with similar surface warming signals can exhibit divergent heat transfer patterns below the sea surface. Accurately identifying MHW processes therefore requires moving beyond surface-focused analyses toward approaches that resolve vertical structures and the components of advection, treating MHWs as three-dimensional phenomena rather than as surface or mixed-layer thermal events.

Methods

Data

We utilized the Global Ocean Physics Reanalysis (GLORYS), an eddy-resolving global ocean reanalysis developed by the Copernicus Marine Environment Monitoring Services (CMEMS). Daily mean potential temperature (hereafter referred to as "temperature"), meridional and zonal velocity components, and mixed layer depth covering a 33-year period from 1993 to 2025 were extracted. The GLORYS dataset has a horizontal resolution of 0.083°×0.083° (approximately 8 km) and consists of 50 vertical levels. We used daily surface flux data (latent and sensible heat flux, shortwave and longwave radiation) from ERA5, the fifth generation European Centre for Medium-Range Weather Forecasts (ECMWF) atmospheric reanalysis, which has a horizontal resolution of 0.25°×0.25°. Additionally, we collected daily sea surface temperature (SST) data from the high-resolution, satellite-based Optimum Interpolation Sea Surface Temperature (OI SST) v2.1 product provided by the National Oceanic and Atmospheric Administration (NOAA), which has a horizontal resolution of 0.25°×0.25°. To validate the GLORYS reanalysis results, in situ temperature profiles were collected from the serial oceanographic observation data of the National Institute of Fisheries Science (NIFS), provided by the Korea Oceanographic Data Center (KODC). The NIFS dataset consists of ship-based hydrographic observations conducted at approximately two-month intervals. The in situ data are measured at specific standard depths (e.g., 0, 10, 20, 30, 50, 75, 100, 150, and 200 m). The overall proportion of missing data in the in situ temperature profiles over the 1993-2025 period is approximately 1%.

The study area spans 128°–131.5°E and 36°–38.5°N (Fig. 1), indicated by a red box superimposed on the General Bathymetry Chart of the Oceans (GEBCO)'s gridded bathymetry map. This region encompasses the Ulleung Basin and is influenced by major boundary currents, including the Tsushima Warm Current (TWC), its branch the East Korea Warm Current (EKWC), and the North Korea Cold Current (NKCC). All datasets utilized in this study were constrained to and analyzed within this specified domain. The spatial extent of the study area was selected to encompass the NIFS transect stations (indicated by white dots) corresponding to observation lines 102–107.

Detrending

To remove the long-term trend associated with global warming, many studies have employed linear regression methods such as ordinary least squares regression. However, temperature time series are generally nonlinear and nonstationary. Applying linear regression to such data can underestimate or overestimate the actual temperature variations, particularly during periods of accelerated warming. Therefore, we adopted the seasonal-trend decomposition using LOESS (STL) to ensure accurate detrending. This non-parametric method decomposes a time series into trend (T_t), seasonal (S_t), and residual (Res_t) components using local regression (LOESS) smoothing, expressing the original series as the sum of these three components[36].

Instead of fitting a single regression equation to the entire period, LOESS estimates a smooth curve by assigning greater weight to localized data points around each time step. To remove the trend component using STL, we applied an 11-year window to extract and eliminate the long-term warming signal. The STL method is robust to outliers and does not assume a linear trend, enabling the extraction

of nonlinear long-term changes. Moreover, in contrast to moving averages, it preserves data at both ends of the time series. Previous studies have demonstrated that this method estimates long-term temperature trends more accurately than linear regression[37,38]. We independently applied the STL procedure to the SST from OI SST and to the temperature, zonal velocity, and meridional velocity from GLORYS.

Marine heatwaves

MHWs were identified based on the definition by Hobday et al.[10]. An MHW is defined as an event where the daily temperature exceeds the local seasonal climatological 90th percentile threshold for at least five consecutive days. Events separated by two or fewer days of temperatures below the threshold are combined into a single, continuous event. The climatological temperature and the 90th percentile threshold for each day of the year are calculated using an 11-day window centered on that day, spanning all available years. The resulting daily climatology and threshold are then smoothed by applying a 31-day moving average.

In this study, surface MHWs in the southwestern East Sea were extracted from daily OI SST data during the warm season (May–September) of 1993–2025. MHWs were identified relative to a fixed climatological baseline[10]. The baseline was defined as the World Meteorological Organization (WMO) standard climate normal (1991–2020)[39], restricted to the period covered by the GLORYS used for the heat budget analysis. GLORYS begins in 1993 with the onset of systematic satellite altimetry assimilation; although OI SST is available from 1982, the same 1993–2020 baseline was applied to both datasets so that MHW detection and the heat budget analysis share an identical reference state. The resulting 28-year baseline is slightly shorter than the recommended 30 years; however, baselines as short as 10 years have been shown to yield MHWs with durations and intensities comparable to those based on 30 years[40].

Furthermore, to capture regionally coherent warming rather than localized variations, MHWs were defined based on the domain-averaged SST. We calculated the MHW characteristics, including frequency, duration, cumulative intensity, and maximum intensity. Duration is defined as the total number of days between the start and end of an MHW event, and cumulative intensity is the sum of daily SST anomalies over the duration of the event. Maximum intensity represents the highest daily SST anomaly recorded during the event.

To assess whether individual MHWs fall within the composite periods, we compared the onset and end of each event with the pre-peak and post-peak periods (Supplementary Fig. S5). The peak period was excluded because every event includes its peak day. An event was considered to cover a period when it occupied at least half of it, that is, when its onset or end lay at least 10 days from the peak day. Events extended from as early as 19 days before to as late as 27 days after the peak day. Only six events covered the pre-peak period, and 10 covered the post-peak period. Because most events covered neither period, composites for these periods reflect not only the development and decay of MHWs but also the conditions preceding and following them.

K-means clustering

K-means clustering[41] is an unsupervised learning method that classifies a dataset into *K* groups based on similarity. The objective of K-means clustering can be expressed as follows:

$$\min_{\{S_k\}_{k=1}^{K}} \sum_{k=1}^{K} \sum_{x_i \in S_k} \|x_i - \mu_k\|^2 \quad (1)$$

where S_k is the set of values assigned to cluster k, and μ_k is the centroid of the cluster. The centroid is calculated as the mean of all values assigned to that cluster:

$$\mu_k = \frac{1}{|S_k|} \sum_{x_i \in S_k} x_i \quad (2)$$

This method assigns each value to the nearest cluster centroid and then updates each centroid with the mean of the values within that cluster. These two steps are repeated until the cluster assignments no longer change or the algorithm reaches convergence. Ultimately, K-means clustering minimizes the within-cluster sum of squared distances.

We employed K-means clustering to classify surface MHWs based on their vertical structures. Following Saranya and Nam[19], a series of domain-averaged temperature anomaly profiles spanning ±30 days centered on the MHW peak day was constructed for each event and used as the input for clustering. As the reanalysis provides continuous profiles, utilizing this temporal window allows the classification to fully incorporate the evolution of the vertical structures associated with MHWs. The number of clusters was set to $k = 4$, thereby classifying MHWs into four types based on their vertical structures.

To validate the classification results derived from the GLORYS dataset, we utilized independent in situ observation profiles from NIFS for comparison and verification. To this end, temperature anomaly profiles for each MHW type were examined using the NIFS serial oceanographic observation data. For each event, an event-specific profile was constructed by spatially averaging at standard depths from all stations along lines 102–107, sampled within ±30 days of the peak day. This composite profile for each type was obtained by averaging the profiles within that type, and the 95% confidence intervals were calculated using a bootstrap approach.

Vertically resolved heat budget

To elucidate the vertical structure of the heat transfer factors associated with MHWs, the depth-resolved full heat budget was defined as:

$$\frac{\partial \theta}{\partial t} = q_{lateral} + q_{sfc} + R \quad (3)$$

where θ is the temperature, $q_{lateral}$ is the temperature tendency from lateral heat flux (oceanic forcing), q_{sfc} is the tendency from surface heat flux (atmospheric forcing), and R is the residual. All terms are calculated layer by layer in units of °C·day^{-1}. Unlike conventional 1D bulk mixed layer models, applying the budget to discrete depth layers allows us to capture subsurface warm anomalies below the mixed layer. The R implicitly includes vertical mixing, vertical heat exchange, entrainment, and horizontal diffusion; thus, its magnitude also serves as an indicator of budget closure.

$q_{lateral}$ is the lateral heat flux through the boundaries of each depth layer, normalized by the layer volume. By adopting a boundary flux form rather than an advective form to analyze net heat exchange, $q_{lateral}$ is expressed as:

$$q_{lateral} = -\frac{1}{A}\oint_{\partial\Omega} \theta\mathbf{v}\cdot\hat{n}\, dl \tag{4}$$

where Ω is the horizontal cross-section at depth z, A is the effective horizontal area bounded by bathymetry, $\mathbf{v}$ is the horizontal velocity vector, and n is the outward normal vector. The reference temperature was set to 0℃ since the net volume transport across the domain boundaries approaches zero (mean -1.6×10^{-3} Sv).

For q_{sfc}, we assumed that the surface heat flux is distributed uniformly down to the mixed layer depth (h):

$$q_{sfc} = \frac{Q_{net}}{\rho_0 c_{p0} h}\mathcal{H}(h-z) \tag{5}$$

where Q_{net} is the net surface heat flux, and $\mathcal{H}$ is the step function. ρ_0=1,025 kg m^{-3} and c_{p0}=4,000 J kg^{-1}K^{-1} are the seawater density and specific heat capacity, respectively. h was defined as the depth at which the potential density exceeds its 10 m value by the amount equivalent to a 0.2 ℃ temperature decrease under the local temperature and salinity at 10 m, as provided in the GLORYS product. Although the q_{sfc} depends on this choice[26], the lateral heat flux is calculated independently at each depth level and is therefore unaffected. By definition, q_{sfc} is zero below the mixed layer, leaving subsurface temperature changes to be governed solely by lateral flow and the residual.

To evaluate MHWs as anomalous extremes, the full heat budget was converted into an anomalous heat budget based on climatology. The temperature flux ($\theta\mathbf{v}$) was decomposed using Reynolds decomposition to isolate the specific components driving the temperature changes. The anomalous lateral heat flux ($q'_{lateral}$) is expressed as:

$$q'_{lateral} = q'_{dyn} + q'_{thermo} + q'_{nonlinear} \tag{6}$$

The three components are formally defined as:

$$\begin{gathered} q'_{dyn} \equiv -\frac{1}{A}\oint \bar{\theta}\mathbf{v}'\cdot\hat{n}\, dl, \qquad q'_{thermo} \equiv -\frac{1}{A}\oint \theta'\bar{\mathbf{v}}\cdot\hat{n}\, dl, \\ q'_{nonlinear} \equiv -\frac{1}{A}\oint (\theta'\mathbf{v}' - \overline{\theta'\mathbf{v}'})\cdot\hat{n}\, dl \end{gathered} \tag{7}$$

where q'_{dyn} is the dynamical component (anomalous velocity acting on mean temperature), q'_{thermo} is the thermodynamical component (incoming anomalous temperature acting on mean velocity), and $q'_{nonlinear}$ is the nonlinear component where both deviate simultaneously.

The final anomalous heat budget is thus given by:

$$\frac{\partial\theta'}{\partial t} = q'_{dyn} + q'_{thermo} + q'_{nonlinear} + q'_{sfc} + R' \tag{8}$$

While the full heat budget quantifies the absolute temperature change driven by each factor, the anomalous budget isolates the intensity of the forcing relative to the climatological norm. Both budgets were calculated daily for each MHW event, aligned to the MHW peak day (±30 days), and composited by MHW type with 95% bootstrap confidence intervals.

Data availability

The datasets analyzed for this study can be found in the Copernicus Marine Service (GLORYS data:

https://data.marine.copernicus.eu/product/GLOBAL_MULTIYEAR_PHY_001_030/description), the Korea Oceanographic Data Center (NIFS serial oceanographic observation data: https://www.nifs.go.kr/kodc/en/observe/line/data), the ECMWF (ERA5 data: https://cds.climate.copernicus.eu/datasets/derived-era5-single-levels-daily-statistics?tab=overview) and the NOAA (OI SST v2.1 data, DOI: https://doi.org/10.25921/RE9P-PT57; data archive: https://www.ncei.noaa.gov/data/sea-surface-temperature-optimum-interpolation/v2.1/access/avhrr/).

References

1. Holbrook, N. J. *et al.* Keeping pace with marine heatwaves. *Nat. Rev. Earth. Environ.* **1**, 482–493 (2020).
2. Wernberg, T., Smale, D. A., Frölicher, T. L. & Smith, A. J. P. ScienceBrief Review: Climate change increases marine heatwaves harming marine ecosystems. in *Critical Issues in Climate Change Science* (eds Liss, P., Le Quéré, C. & Forster, P.) (Zenodo, 2021). doi:https://doi.org/10.5281/zenodo.5596820.
3. Smith, K. E. *et al.* Biological impacts of marine heatwaves. *Annu. Rev. Mar. Sci.* **15**, 119–145 (2023).
4. Oliver, E. C. J. *et al.* Longer and more frequent marine heatwaves over the past century. *Nat. Commun.* **9**, 1324 (2018).
5. Lee, E.-Y. & Park, K.-A. Change in the recent warming trend of sea surface temperature in the East Sea (Sea of Japan) over decades (1982–2018). *Remote Sens.* **11**, 2613 (2019).
6. Lee, S. *et al.* Rapidly changing East Asian marine heatwaves under a warming climate. *J. Geophys. Res. Oceans.* **128**, e2023JC019761 (2023).
7. Wang, Q. *et al.* Properties and drivers of marine heat waves in the Northern South China Sea. *J. Phys. Oceanogr.* **52**, 917–927 (2022).
8. Park, S. & Kim, K. Depth- and season-resolved characteristics and drivers of marine heatwaves in the East Sea (Sea of Japan). *Mar. Environ. Res.* **211**, 107418 (2025).
9. Kim, H.-J., Lee, D. E., Lee, E. Y., Baek, H. & Park, Y.-G. The role of upper ocean stratification in resurgent marine heatwaves in the East/Japan Sea. *Sci. Rep.* **16**, 17933 (2026).
10. Hobday, A. J. *et al.* A hierarchical approach to defining marine heatwaves. *Prog. Oceanogr* **141**, 227–238 (2016).
11. Oliver, E. C. J. Mean warming not variability drives marine heatwave trends. *Clim. Dyn.* **53**, 1653–1659 (2019).
12. Capotondi, A. *et al.* A global overview of marine heatwaves in a changing climate. *Commun Earth Environ* **5**, 701 (2024).
13. Smith, K. E. *et al.* Baseline matters: Challenges and implications of different marine heatwave baselines. *Prog. Oceanogr* **231**, 103404 (2025).
14. Chiswell, S. M. Global trends in marine heatwaves and cold spells: The impacts of fixed versus changing baselines. *J. Geophys. Res. Oceans.* **127**, e2022JC018757 (2022).
15. Xu, T. *et al.* An increase in marine heatwaves without significant changes in surface ocean temperature variability. *Nat Commun* **13**, 7396 (2022).
16. Elzahaby, Y., Schaeffer, A., Roughan, M. & Delaux, S. Oceanic circulation drives the deepest and longest marine heatwaves in the East Australian current system. *Geophys. Res. Lett.* **48**, e2021GL094785 (2021).
17. Martínez, J. *et al.* Evolution of marine heatwaves in warming seas: the Mediterranean Sea case study. *Front. Mar. Sci.* **10**, 1193164 (2023).

18. Zhang, Y., Du, Y., Feng, M. & Hobday, A. J. Vertical structures of marine heatwaves. *Nat Commun* **14**, 6483 (2023).
19. Saranya, J. S. & Nam, S. Subsurface evolution of three types of surface marine heatwaves over the East Sea (Japan Sea). *Prog. Oceanogr* **222**, 103226 (2024).
20. Li, Z. *et al.* Characteristics and mechanisms of summer subsurface marine heatwaves in the East/Japan Sea. *Front. Mar. Sci.* **12**, 1680577 (2025).
21. Richaud, B. *et al.* Drivers of marine heatwaves in the Arctic Ocean. *J. Geophys. Res. Oceans.* **129**, e2023JC020324 (2024).
22. Vogt, L., Burger, F. A., Griffies, S. M. & Frölicher, T. L. Local drivers of marine heatwaves: A global analysis with an Earth system model. *Front. Clim.* **4**, 847995 (2022).
23. Holbrook, N. J. *et al.* A global assessment of marine heatwaves and their drivers. *Nat Commun* **10**, 2624 (2019).
24. Bian, C. *et al.* Oceanic mesoscale eddies as crucial drivers of global marine heatwaves. *Nat Commun* **14**, 2970 (2023).
25. Sala, J., Giglio, D., Capotondi, A., Sukianto, T. & Kuusela, M. Leading dynamical processes of global marine heatwaves in an ocean state estimate. *Ocean Sci.* **21**, 2463–2479 (2025).
26. Elzahaby, Y., Schaeffer, A., Roughan, M. & Delaux, S. Why the mixed layer depth matters when diagnosing marine heatwave drivers using a heat budget approach. *Front. Clim.* **4**, 838017 (2022).
27. Liang, X., Wunsch, C., Heimbach, P. & Forget, G. Vertical redistribution of oceanic heat content. *J. Clim.* **28**, 3821–3833 (2015).
28. Roberts, C. D. *et al.* Surface flux and ocean heat transport convergence contributions to seasonal and interannual variations of ocean heat content. *J. Geophys. Res. Oceans.* **122**, 726–744 (2017).
29. Oldenburg, D. *et al.* The respective roles of ocean heat transport and surface heat fluxes in driving Arctic Ocean warming and sea ice decline. *J. Clim.* **37**, 1431–1448 (2024).
30. Usui, N. & Hirose, N. Interannual to decadal variability of ocean heat content in the Japan Sea: Role of the Tsushima Warm Current and its relation to the Kuroshio extension variability. *J. Clim.* **38**, 3593–3607 (2025).
31. Roewer, S., Fiedler, L., Årthun, M., Huiskamp, W. & Rahmstorf, S. Nordic overturning increases as AMOC weakens in response to global warming. *Ocean Sci.* **22**, 1195–1211 (2026).
32. Frankignoul, C. Sea surface temperature anomalies, planetary waves, and air-sea feedback in the middle latitudes. *Rev. Geophys.* **23**, 357–390 (1985).
33. Park, S., Deser, C. & Alexander, M. A. Estimation of the surface heat flux response to sea surface temperature anomalies over the global oceans. *J. Clim.* **18**, 4582–4599 (2005).
34. Zhang, R., Cheng, Y. & Wang, X. Classification of marine heatwaves in the South China Sea and their thermodynamic features. *Atmospheric and Oceanic Science Letters* **19**, 100662 (2026).
35. Lee, E.-J., Hwang, Y., Kim, Y.-T., Nam, S. & Park, J.-H. Data-driven multidecadal reconstruction and nowcasting of coastal and offshore 3-D sea temperature fields from satellite observations: A case study in the East/Japan Sea. *Remote Sens.* **18**, 246 (2026).
36. Cleveland, R. B., Cleveland, W. S., McRae, J. E. & Terpenning, I. STL: A seasonal-trend decomposition procedure based on loess. *J. Off. Stat.* **6**, 3–73 (1990).
37. Chang, M.-H. *et al.* Revisiting regression methods for estimating long-term trends in sea surface temperature. *Nat. Hazards Earth Syst. Sci.* **24**, 2481–2494 (2024).
38. Paradan, A. F., Gafoor, F. A. & AlShehhi, M. R. Intensification of marine heatwaves and their climate drivers in the Arabian Gulf. *Sci. Rep.* **15**, 34506 (2025).
39. *Guide to Climatological Practices*. (World Meteorological Organization, Geneva, Switzerland, 2018).

40. Schlegel, R. W., Oliver, E. C. J., Hobday, A. J. & Smit, A. J. Detecting marine heatwaves with sub-optimal data. *Front. Mar. Sci.* **6**, 737 (2019).
41. Macqueen, J. Some methods for classification and analysis of multivariate observations. in vol. 1 281–297 (University of California Press, Berkeley, CA, 1967).

Author contributions

J.H.L. conceived the study, analyzed the data, prepared the figures, and wrote the original draft. C.H.K. validated the methodology. D.Y.K. conceived the study and administered the project. Y.S.C. reviewed and wrote the manuscript. All authors read and approved the final manuscript.

Funding

This research was supported by Korea Institute of Marine Science & Technology Promotion (KIMST) funded by the Korea Coast Guard (RS-2022-KS221629).

Competing interests

The authors declare no competing interests.

Supplementary Files

This is a list of supplementary files associated with this preprint. Click to download.

- SupplementaryMaterial.pdf